Integration of Microspheres and Multi-Quantum-Well Modulators as Retro-Modulation Surfaces for Optical Wireless and Free-Space Optical Communication

Alexander C. MacGillivray[1], *Graduate Student Member, IEEE*, Mathew W. Bishop[1], *Student Member, IEEE*, Benjamin C. Maglio[2], Samuel Shutts[3], Peter M. Smowton[3], *Senior Member, IEEE*, and Jonathan F. Holzman[1], *Member, IEEE*

***Abstract*—In this work, we introduce a retro-modulator surface as a monolithic passive transceiver for optical wireless and free-space optical communication links. It incorporates a sublayer of microspheres for retroreflection, and a multi-quantum-well (MQW) structure for modulation over the optical communication C-band (1530–1565 nm) when driven by digital voltages (0–5 V). Our theoretical analyses suggest that LaSFN9 and $BaTiO_3$ microspheres, with refractive indices of 1.8 and 2.0, respectively, give optimal retroreflection for short and long link lengths, respectively, while our experimental analyses show that our AlGaInAs-based MQW modulator imparts sufficiently deep modulation over the C-band. This has our integrated retro-modulator surfaces with LaSFN9 or $BaTiO_3$ microspheres function with fields-of-view of 10.8° or 9.4°, respectively, and modulation depths of 3.4% or 5.3%, respectively. Our characterizations of error performance through links exhibiting weak, moderate, and strong turbulence then show error vector magnitudes of 3.7%, 9.2%, and 24%, respectively, with bit error rates below 10^{-3}, below 10^{-3}, and equal to 0.0183, respectively. Ultimately, we conclude that the retro-modulator surfaces can function effectively as passive transceivers for optical wireless or free-space optical communication links, through weak or moderate turbulence, while offering minimal size, weight, and power.**

***Index Terms*—Free-space optical communications, multi-quantum-well, retroreflection, electroabsorption modulators**

I. INTRODUCTION

Optical wireless and free-space optical (FSO) communication systems have seen growing interest, given their enabling of high data rates and wireless connectivity [1–3]. This has led to numerous efforts and achievements for optical wireless communications, over (shorter) indoor [4] and terrestrial [5] links, and FSO communications, over (longer) aerial [6] and aerospace [7] links. The efforts have been directed at both the transceivers, to have them function effectively in the desired optical spectrum, and the overall links, which must accommodate the multidirectionality of wireless/free-space environments. These demands have been met to date by traditional *active-active links* [8] having *active transceivers* [9] at opposing ends of the links. Each active transceiver then incorporates a laser source, to transmit the encoded beam, and (potentially) adaptive optics, to maintain the beam's alignment to the opposing end. Unfortunately, it can be difficult to implement such active-active links when mobility is required at an end of the link. This is because the active transceivers' lasers and adaptive optics often have size, weight, and power (SWaP) beyond the ubiquitous SWaP [10] constraints in mobile links.

Given the demands of active transceivers in active-active links, and the growing interest in mobile deployments, various forms of *passive transceivers* have been developed for *active-passive links* [5,11]. Passive transceivers function with retroreflectors and modulators, whereby the retroreflectors redirect incident laser beams back to their sources (active transceivers), and the modulators encode data onto the returning beams. This allows active-passive communication links to be established between (fixed) active transceivers and (mobile) passive transceivers. Such a scheme allows each passive transceiver to function with minimal SWaP, given its lack of laser and adaptive optics, while offering alignment insensitivity, due to the multidirectional nature of retroreflection. Various forms of retroreflectors and modulators have been developed for such passive transceivers, by us [12,13] and others [14–17], and the proposed work furthers these efforts.

In the proposed work, we introduce a retro-modulator surface as a monolithic passive transceiver, with scalable size, minimal weight, and low power consumption. The surface incorporates a sublayer of microspheres, for retroreflection over a broad field-of-view, and an overlying multi-quantum-well (MQW) modulator. The MQWs consist of quaternary III–V alloys based on varying compositions of AlGaInAs material with well/barrier widths of 6 nm/9 nm and *n*- and *p*-type InP cladding layers. The structure is engineered for deep modulation in the optical communication C-band (1530–1565 nm), while driven by digital voltages (0–5 V).

We put forward a theoretical analysis of the retroreflection, based upon Mie and ray theories, and an experimental analysis of the modulation, as a function of wavelength and voltage. We

Manuscript received ???, 2025; accepted ???, 2025. Date of publication ???, 2025; date of current version ???, 2025. This work was supported by the Natural Sciences and Engineering Research Council of Canada (NSERC) under grants RGPIN-2023-04407 and ALLRP-597785-24, the Canada Foundation for Innovation (CFI) under grants 16659 and 43542, and Western Economic Diversification Canada. (Corresponding author: Jonathan F. Holzman.)

The authors are with the [1]School of Engineering at the University of British Columbia, Kelowna, British Columbia, Canada, V1V 1V7 (e-mail: jonathan.holzman@ubc.ca), [2]Institute of Arctic Biology, University of Alaska Fairbanks, Fairbanks, AK 99775, United States, and [3]School of Physics and Astronomy, Cardiff University, The Parade, Cardiff CF24 3AA, United Kingdom

Color versions of one or more of the figures in this article are available online at http://ieeexplore.ieee.org.

then present device characterizations of the retro-modulator surface, as received power versus incident angle, given LaSFN9 (Schott glass) and $BaTiO_3$ (barium titanate glass) microspheres in the sublayer and low (0 V) and high (5 V) voltages applied across the MQWs. The results show that our LaSFN9/$BaTiO_3$-based microspheres and AlGaInAs-based MQW modulator, together, can give the desired broad field-of-view and deep modulation. Moreover, the device's planar topology allows it to be scaled in surface area, as desired, with negligible increases to its weight and power. This can make the retro-modulator surface an effective monolithic technology for mobile transceivers in future optical wireless and FSO communication links.

II. Theoretical and Experimental Analyses

A schematic of the retro-modulator surface is shown in Fig. 1(a). The structure incorporates a sublayer of microspheres, to retroreflect the incident optical beam, and a MQW modulator, sandwiched between the displayed glass layers and indium tin oxide (ITO) films. A voltage V is applied to the ITO films to induce a reverse bias across the MQWs and thereby increase absorption of the optical beam as it undergoes a roundtrip through the structure. The structure's retroreflection is established by refraction in the microspheres, according to their diameter d and refractive index n, while its modulation is defined by the quantum-confined Stark effect [18] in the MQW modulator, near the (free-space) wavelength $\lambda_0 = 1550$ nm.

The retro-modulator surface is characterized by the experimental setup shown in Fig. 1(b). Its laser beam reflects off beamsplitter BS (Newport Corp., 20B20BS.3) and then the retro-modulator surface (Thorlabs Inc., XYR1/M). The retro-modulated beam is then transmitted back through beamsplitter BS, focused by the (25.4-mm biconvex) lens, and measured by the photodiode (Thorlabs Inc., DET20C/M), for various values of incident angle θ on the retro-modulator surface. The following subsections give a theoretical analysis of the retroreflection and an experimental analysis of the modulation.

A. Theoretical Analysis of Retroreflection

In this subsection, we put forward a theoretical analysis of retroreflection from the microspheres. In doing so, we recognize that effective retroreflection requires each microsphere to focus incident optical power onto its rear vertex, at the intersection of the optical axis and surface, and then recollimate the reflected power for propagation to (and captured by) the receiver. The effectiveness here is characterized by the retroreflectance $R_R(n,\theta)$, being the fraction of retroreflected to incident power within an acceptable cone of divergence angles [19]. For this work's experimental setup, with a 0.4-m link length and 25.4-mm aperture diameter for the receiver, retroreflected rays with divergence angles up to roughly 3.6° are acceptable, as they are captured by the receiver's aperture. Thus, retroreflectance in our work conveys the fraction of power on each microsphere that gets effectively focused, onto its rear vertex, and recollimated, for capture by the receiver. The microsphere's refractive index n and the incident angle θ play key roles in defining this fraction and the overall retroreflectance $R_R(n,\theta)$.

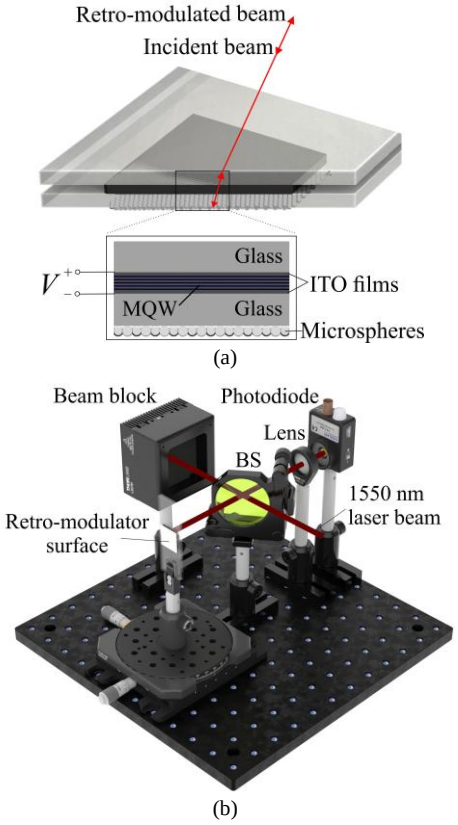

Fig. 1. Schematic of the retro-modulator surface and experimental setup. In (a), the retro-modulator surface is shown with its integrated sublayer of microspheres and multi-quantum-well (MQW) modulator. The latter is sandwiched between glass layers and indium tin oxide (ITO) films. A voltage V is applied to the ITO films to form a reverse bias across the MQW modulator. In (b), the experimental setup that characterizes the retro-modulator surface is shown. Its 1550-nm laser beam reflects off beamsplitter BS, reflects off the retro-modulator surface, passes through beamsplitter BS, is focused by the lens, and is measured by the photodiode, at varied incident angles on the retro-modulator surface.

The black curve in Fig. 2(a) shows the normalized retroreflectance $R_R(n,\theta)$, on the left axis, as a function of the microsphere's refractive index n, at an incident angle of $\theta = 0°$. The results are generated from a ray theory analysis with a microsphere diameter of $d = 56$ μm, a free-space wavelength of $\lambda_0 = 1550$ nm, and the aforementioned link length and receiver aperture. The results show that a refractive index of $n \approx 1.9$ will maximize the retroreflectance. We can interpret this maximum as a compromise between optimal focusing onto the rear vertex (at lower refractive indices) and optimal recollimation towards the receiver (at higher refractive indices).

The two grey curves in Fig. 2(a) illustrate this compromise by way of results for the normalized focal intensity at the rear vertex, on the right axis, as a function of the microsphere's refractive index n. The leftmost grey curve is the result of Mie theory analysis [20], following our prior work [21], and so it presents exact solutions to Maxwell's equations in the microsphere. Such results suggest that a microsphere with a refractive index of $n \approx 1.8$ can collect and focus the greatest fraction of its incident power onto the rear vertex, as a so-called photonic nanojet [22]. However, such a microsphere would then retroreflect this power with relatively large divergence and poor

recollimation, limiting its use for short link lengths. The rightmost curve comes about from a ray theory analysis with only paraxial rays. It shows the well-known result that a microsphere with a refractive index of $n \approx 2.0$ can collect and focus incident power from its paraxial area onto the rear vertex [23]. Its retroreflected power is then well-collimated, in support of long link lengths.

Overall, our theoretical results show that microspheres can be applied to retroreflection given attention to the link length. For short links, the microspheres have an optimal refractive index that is relatively low and diameter dependent. Given the microsphere diameter of $d = 56$ μm in this work, the optimum is $n \approx 1.8$. In contrast, for long links, the microspheres will have an optimal refractive index that is simply fixed at $n \approx 2.0$. Given these limits, the rest of this work will characterize retro-modulator surfaces with sublayers of LaSFN9 microspheres, whose diameter $d \approx (54 \pm 9)$ μm and refractive index $n \approx 1.8$ mimic the former case, and $BaTiO_3$ microspheres, whose diameter $d \approx (58 \pm 5)$ μm and refractive index $n \approx 2.0$ mimic the latter case.

B. Experimental Analysis of Modulation

In this subsection, we put forward an experimental analysis of modulation. The experiment was conducted by measuring the transmitted spectra through a single pass of the MQW modulator, while voltages of $V = 0$ and 5 V are applied. This uses a broadband light-emitting diode (Thorlabs Inc., M1550L3) as the spectral source and an optical spectrum analyzer (Yokogawa Test & Measurement Corp., AQ6370) as the detector.

Fig. 2(b) shows results for the modulator's absorptance $A_M(V, \theta = 0°)$ as a function of wavelength λ_0 under low ($V = 0$ V, blue) and high ($V = 5$ V, red) voltage states, with markers for the experimental data and lines for fitted curves. Overall, the results exhibit a staircase response for absorption, with downward steps for increasing wavelength. This observation aligns with the expected staircase characteristics of quantum wells, for which increasing photon energy (and decreasing wavelength) yields upward steps in the density of states (and thus absorption) [24]. Sharp peaks are absent at the steps' edges, suggesting that exciton resonance contributions are negligible in our room-temperature measurements. Modulation is characterized predominantly by the redshifting of transition energies, though there is an overall increase in absorptance across the spectrum, which suggests overlap between the broadened transition energy states as they approach. In terms of modulation, we see our 5-V increase in voltage raise the absorptance by 0.10% at the lower edge of the C-band (1530 nm), 0.20% near the centre of the C-band (1550 nm), and 0.13% at the upper edge of the C-band (1565 nm). Across the full C-band, the absorptance change is characterized by an average of 0.17%. We consider this to be sufficiently deep voltage-induced modulation, as the retro-modulator surface has the beam make a roundtrip through the MQW modulator (and thus enhance this modulation).

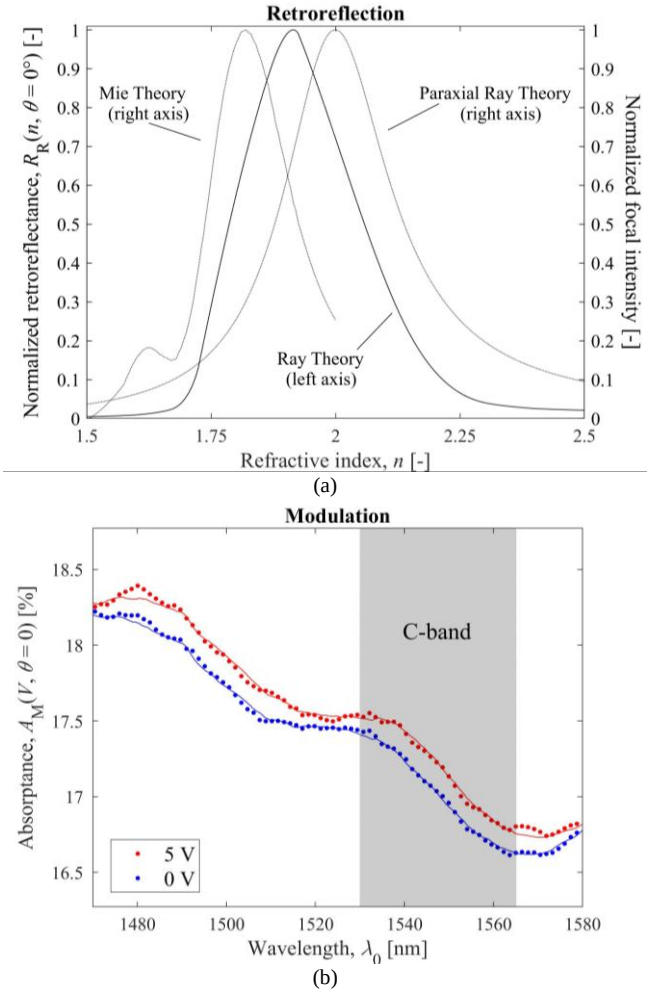

Fig. 2. Retroreflection and modulation analyses of the microspheres and multi-quantum-well (MQW) modulator, respectively. In (a), theoretical results for the normalized retroreflectance $R_R(n, \theta = 0°)$ of a microsphere is shown as a black curve, mapped to the left axis, while theoretical results for the normalized focal intensity at the microsphere's rear vertex are shown as grey curves, mapped to the right axis. The former (black) curve is generated from a ray theory analysis; the latter (grey) curves are generated from Mie theory and paraxial ray theory analyses. Results are shown as a function of the microsphere's refractive index n, given a diameter of d = 56 μm and free-space wavelength of λ_0 = 1550 nm. In (b), experimental results are shown for the absorptance $A_M(V, \theta = 0°)$ from a single pass through the MQW modulator as a function of free-space wavelength λ_0 under low (V = 0 V, blue) and high (V = 5 V, red) voltage states. The optical communication C-band is shaded in grey.

III. Integrated Device Characterization

In this section, we draw upon the prior theoretical and experimental analyses in characterizing the full retro-modulator surface. In doing so, we recognize that its received power, relative to the incident power P_{inc} = 1.5 mW (1.76 dBm), manifests as a product of *i.* the microsphere sublayer's retroreflectance, and *ii.* the MQW modulator's transmittance squared, given that the beam passes twice through the modulator. We expand upon these two factors here.

i. The retroreflectance of the microsphere sublayer $R_R(n, \theta)$ is defined in our work as a ratio of the received power (at our receiver) to the incident power (on the sublayer), while neglecting the MQW modulator. It is governed by the refractive index n of

the arrayed microspheres in the sublayer and the incident angle θ of the beam on the retro-modulator surface, according to

$$R_{\mathrm{R}}(n,\theta) \approx R_{\mathrm{MS}} T_{\mathrm{MS}}^2 (A_{\mathrm{PX}}(n)/A_{\mathrm{MS}})(A_{\mathrm{MS}}/A_{\mathrm{UC}}) \times \exp(-4\ln(2)\theta^2/\sigma_{\mathrm{R}}^2). \quad (1)$$

Here, $R_{\mathrm{MS}} \approx 0.33$ is each microsphere's (rear surface) reflectance and $T_{\mathrm{MS}} \approx 0.92$ is each microsphere's (front surface) transmittance, approximated from the refractive indices of our LaSFN9 ($n \approx 1.8$) and $BaTiO_3$ ($n \approx 2.0$) microspheres. The area $A_{\mathrm{PX}}(n)$ is the paraxial (circular) area centred on each microsphere's greater (circular) cross-section A_{MS} within which all incident rays will be captured by the receiver's aperture. Thus, the ratio $A_{\mathrm{PX}}(n)/A_{\mathrm{MS}}$ can be interpreted as the fraction of incident optical power on each microsphere that will be captured by the receiver's aperture, while neglecting reflective/absorptive losses and the MQW modulator. From our ray-based analysis, the LaSFN9 and $BaTiO_3$ microspheres yield paraxial cross-sectional areas of $A_{\mathrm{PX}}(n{=}1.8) \approx 0.21d^2$ and $A_{\mathrm{PX}}(n{=}2.0) \approx 0.27d^2$, respectively, and ratios of $A_{\mathrm{PX}}(n{=}1.8)/A_{\mathrm{MS}} \approx 0.27$ and $A_{\mathrm{PX}}(n{=}2.0)/A_{\mathrm{MS}} \approx 0.34$, respectively, given each microsphere's diameter $d \approx 56$ μm and total cross-sectional area $A_{\mathrm{MS}} = (\pi/4)d^2 \approx 0.79d^2$. (See Appendix A for further details on this ray-based analysis.) We then recognize that the microspheres are arrayed over two dimensions in a close-packed hexagonal structure. Its primitive unit cell has a rhombic form, with one microsphere in it, and an area of $A_{\mathrm{UC}} = 3^{1/2}d^2/2 \approx 0.87d^2$. This area lets us interpret the ratio $A_{\mathrm{MS}}/A_{\mathrm{UC}} = \pi/(12)^{1/2} \approx 0.91$ above as the fraction of incident optical power on each unit cell that strikes its microsphere. Next, we consider that the microsphere sublayer's overall retroreflectance $R_{\mathrm{R}}(n,\theta)$ will depend upon the incident angle θ of rays on the sublayer, due to shadowing and eclipsing between neighbouring microspheres as the incident angle θ grows. We empirically modelled and fit this dependence by the function $\exp(-4\ln(2)\theta^2/\sigma_{\mathrm{R}}^2)$, whereby angular full-width-at-half-maximum (FWHM) values $\sigma_{\mathrm{R}} = 10.8°$ and 9.4° best characterized the LaSFN9 ($n \approx 1.8$) and $BaTiO_3$ ($n \approx 2.0$) microspheres, respectively. Finally, we use (1) to compute the microsphere sublayer's retroreflectance at normal incidence, giving $R_{\mathrm{R}}(n{\approx}1.8, \theta{=}0°) \approx 0.086$ for the LaSFN9 microspheres and $R_{\mathrm{R}}(n{\approx}2.0, \theta{=}0°) \approx 0.11$ for the $BaTiO_3$ microspheres. Such retroreflectance values convey the fraction of incident optical power on the retro-modulator surface that will be captured by the receiver's aperture, neglecting the MQW modulator, and so the remaining power manifests as power penalties in optical wireless and FSO link budgets.

In interpreting the above parameters for links, we see that the product $R_{\mathrm{MS}}T_{\mathrm{MS}}^2$ gives a power penalty of –5.53 dB, the ratio $A_{\mathrm{PX}}(n)/A_{\mathrm{MS}}$ for LaSFN9 and $BaTiO_3$ microspheres yields power penalties of –5.66 dB and –4.61 dB, respectively, the ratio $A_{\mathrm{MS}}/A_{\mathrm{UC}}$ yields a power penalty of –0.42 dB, and the function of θ yields a power penalty of 0.00 dB at normal incidence. Overall, our retro-modulator surfaces with LaSFN9 and $BaTiO_3$ microspheres give comparable power penalties in FSO links. The roughly 1 dB lower power penalty for $BaTiO_3$ microspheres is due to their larger paraxial area $A_{\mathrm{PX}}(n)$, as this raises their ratio $A_{\mathrm{PX}}(n)/A_{\mathrm{MS}}$ and received power, but further reductions in power penalty will be difficult with just $A_{\mathrm{PX}}(n)$. Instead, efforts could be made to increase the product $R_{\mathrm{MS}}T_{\mathrm{MS}}^2$ and decrease its relatively large power penalty. This could be achieved by metallizing the microspheres' rear surface, for example, as this would raise their low reflectance ($R_{\mathrm{MS}} \approx 0.33$) closer to unity. Such changes could help establish and maintain the operation of links with especially tight power budgets.

ii. The transmittance of the MQW modulator is defined in our work by the ratio of its transmitted power to incident power. It is governed by the applied voltage V and the incident angle θ of the beam on the retro-modulator surface, according to

$$\begin{aligned} T_{\mathrm{MQW}}(V,\theta) &\approx T_{\text{air-gls}}^2 T_{\text{gls-ITO}}^2 T_{\text{ITO-air}}^2 T_{\text{air-InP}}^2 (1-A_{\mathrm{ITO}})^2 (1-A_{\mathrm{M}}(V,\theta)) \\ &= T_{\text{air-gls}}^2 T_{\text{gls-ITO}}^2 T_{\text{ITO-air}}^2 T_{\text{air-InP}}^2 (1-A_{\mathrm{ITO}})^2 \\ &\quad \times \exp(-\alpha(V)t/(1-\sin^2\theta/n_{\mathrm{InP}}^2)^{1/2}). \end{aligned} \quad (2)$$

Here, the MQW modulator incorporates air, glass, ITO, and an InP substructure, with $T_{\text{air-gls}} = 0.97$, $T_{\text{gls-ITO}} = 0.99$, $T_{\text{ITO-air}} = 0.91$, and $T_{\text{air-InP}} = 0.92$ as transmittance values of its air-glass, glass-ITO, ITO-air, and air-InP interfaces, respectively. (Each interface appears twice in the MQW modulator and so each transmittance is squared in (2).) The transmittance $(1-A_{\mathrm{ITO}}) \approx 0.85$ appears due to the nonnegligible absorption of the ITO films at an absorptance of $A_{\mathrm{ITO}} \approx 0.15$ [25], and the transmittance $(1-A_{\mathrm{M}}(V,\theta))$ appears due to the absorption of the InP substructure, at an absorptance of $A_{\mathrm{M}}(V,\theta) = (1-\exp(-\alpha(V)t/(1-\sin^2\theta/n_{\mathrm{InP}}^2)^{1/2}))$. The dependence on applied voltage V is our desired modulation; the dependence on incident angle θ is due to its increase to the propagation length in the InP substructure. Namely, an incident angle θ leads to a transmitted angle of $\arcsin(\sin\theta/n_{\mathrm{InP}})$ and propagation length of $t/(1-\sin^2\theta/n_{\mathrm{InP}}^2)^{1/2}$ through the InP substructure, where the refractive index is $n_{\mathrm{InP}} = 3.3$ and the thickness is $t = 300$ μm. We then extract the absorption coefficient $\alpha(V)$ from our measured results in Fig. 2(b), at an incident angle of $\theta = 0°$, wavelength of $\lambda_0 = 1550$ nm, and applied voltages of $V = 0$ and 5 V. This gives $\alpha(V{=}0\mathrm{V}) = 611\ \mathrm{m}^{-1}$ and $\alpha(V{=}5\mathrm{V}) = 631\ \mathrm{m}^{-1}$, respectively, absorptance values of $A_{\mathrm{M}}(V{=}0\mathrm{V}, \theta{=}0°) = 0.168$ and $A_{\mathrm{M}}(V{=}5\mathrm{V}, \theta{=}0°) = 0.172$, respectively, and transmittance values of $(1-A_{\mathrm{M}}(V{=}0\mathrm{V}, \theta{=}0°)) = 0.83$ and $(1-A_{\mathrm{M}}(V{=}5\mathrm{V}, \theta{=}0°)) = 0.82$, respectively. Finally, we use (2) to compute the MQW modulator's transmittance at normal incidence, giving $T_{\mathrm{MQW}}(V{=}0\mathrm{V}, \theta{=}0°) \approx 0.39$ and $T_{\mathrm{MQW}}(V{=}5\mathrm{V}, \theta{=}0°) \approx 0.38$. As these transmittance values denote the fraction of incident optical power that is transmitted through the MQW modulator, the remaining power, lost by reflections or absorption, manifests as power penalties in the link. Namely, the squared transmittance values $T_{\text{air-gls}}^2$, $T_{\text{gls-ITO}}^2$, $T_{\text{ITO-air}}^2$, $T_{\text{air-InP}}^2$, and $(1-A_{\mathrm{ITO}})^2$ yield power penalties of –0.26 dB, –0.09 dB, –0.78 dB, –0.74 dB, and –1.4 dB, respectively, and the transmittance values $(1-A_{\mathrm{M}}(V{=}0\mathrm{V}, \theta{=}0°))$ and $(1-A_{\mathrm{M}}(V{=}5\mathrm{V}, \theta{=}0°))$ give power penalties of –0.79 dB and –0.82 dB, respectively. Given the comparable power penalties here, there is no one limiting loss factor. However, the MQW modulator's operation could benefit from greater absorptance in its high (5 V) state, ideally with lower absorptance in its low (0 V) state.

Ultimately, the received power $P_{RX}(n,V,\theta)$ from the retro-modulator surface is defined as a product of the incident power P_{inc}, the microsphere sublayer's retroreflectance $R_R(n,\theta)$, and the MQW modulator's transmittance $T_{MQW}(V,\theta)$ squared. This gives

$$\begin{aligned} P_{RX}(n,V,\theta) &= P_{inc}\, R_R(n,\theta) T_{MQW}(V,\theta)^2 \\ &= P_{inc}[R_{MS} T_{MS}^2 (A_{PX}(n)/A_{MS})(A_{MS}/A_{UC}) \\ &\quad \times \exp(-4\ln(2)\theta^2/\sigma_R^2)] \\ &\quad \times [T_{air\text{-}gls}^4 T_{gls\text{-}ITO}^4 T_{ITO\text{-}air}^4 T_{air\text{-}InP}^4 (1-A_{ITO})^4 \\ &\quad \times \exp(-2\alpha(V)t/(1-\sin^2\theta/n_{InP}^2)^{1/2})]. \end{aligned} \quad (3)$$

Fig. 3 presents this received power $P_{RX}(n,V,\theta)$ as theoretical curves, fitted from (3), and experimental markers. Figs. 3(a) and (b) show the results for retro-modulator surfaces with LaSFN9 (n≈1.8) and $BaTiO_3$ (n≈2.0) microspheres, respectively, versus incident angle θ at low (V = 0 V, blue) and high (V = 5 V, red) voltage V states. The received power in the figures shows a strong central lobe, from specular retroreflection of the paraxial optical power off the microsphere sublayer, on top of a weak and broad background pedestal, due to diffuse reflections of nonparaxial optical power off the microsphere sublayer. (We empirically fit the background pedestal by the Lorentzian function $B(\theta) = B_0/(1+(2\theta/\sigma_B)^2)$, where B_0 = 2 μW is its amplitude and σ_B = 50° and 84° are its fitted FWHM values for sublayers with LaSFN9 and $BaTiO_3$ microspheres, respectively.) Ultimately, the theoretical and experimental results for received power $P_{RX}(n,V,\theta)$ show good agreement for the LaSFN9 (n ≈ 1.8) and $BaTiO_3$ (n ≈ 2.0) microspheres, with a field-of-view (FWHM) of 10.8° and 9.4°, and voltage-induced modulation depths (between V = 0 and 5 V) of 3.4% and 5.3%, respectively.

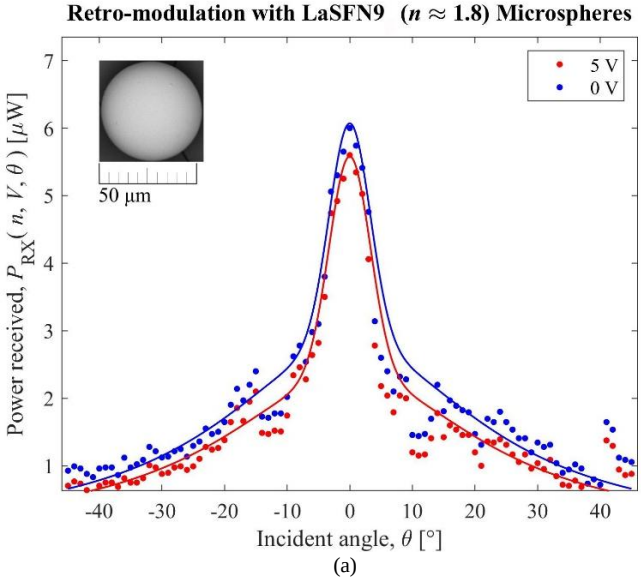

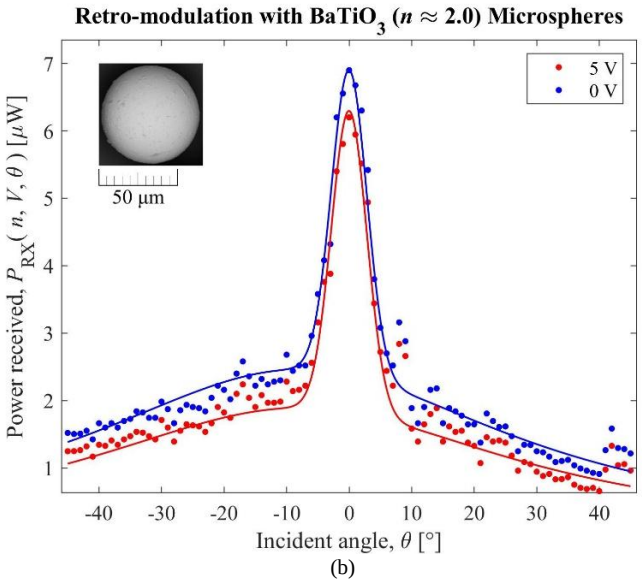

Fig. 3. Retro-modulation characteristics for the retro-modulator surface. Results are shown as received power $P_{RX}(n,V,\theta)$ as a function of incident angle θ, given (a) LaSFN9 and (b) $BaTiO_3$ microspheres in its sublayer, and low (V = 0 V, blue) and high (V = 5 V, red) voltage states across its multi-quantum-well (MQW) modulator. Experimental results are denoted with markers; theoretical fits are denoted with lines. Scanning electron microscope (SEM) images of the microspheres are displayed as insets.

IV. Discussion

Overall, the retro-modulator surface exhibited effective retroreflection and modulation to support its integration in passive transceivers and its application to active-passive optical wireless and FSO communication links.

In seeking effective retroflection, for minimal divergence in the links, we found that combined attention had to be paid to the microspheres' refractive index and link length. For short links, the microspheres' optimal refractive index was relatively low and diameter dependent. (The microsphere diameter in our work, d≈56 μm, had an optimal refractive index of n≈1.8.) For long links, the optimal refractive index became fixed at n≈2.0. We then tested retro-modulator surfaces with LaSFN9 microspheres, whose refractive index (n≈1.8) is at the lower limit, and $BaTiO_3$ microspheres, whose refractive index (n≈2.0) is at the upper limit. The microspheres functioned as expected, but their contributions to the received power would ideally be increased. This could be done by metallizing their rear surfaces, as this would raise their low reflectance (R_{MS} ≈ 0.33) closer to unity and give a proportional increase to the received power.

In seeking an effective modulation depth, we made use of an MQW modulator with AlGaInAs material and well/barrier widths of 6 nm/9 nm. We found it could impart the desired deep modulation from digital voltages (0–5 V) over the optical communication C-band (1530–1565 nm). For a single pass through our MQW modulator, the full C-band showed a voltage-induced change in absorptance of 0.17%. However, it is also worth noting that our characterization of the MQW modulator could show metastable states in its modulation due to temperature dependence in its absorptance. Specifically, a transition to the high voltage state would increase the absorptance, and thus

the absorption of laser power, leading to an increase in the device's temperature. A subsequent transition back down to the low voltage state might not, then, return the device to its initial low voltage state, due to its heightened temperature. We have observed such metastability for electroabsorption in bulk semiconductors, such as semi-insulating InP [26], and have found that it can be lessened by using sufficiently low laser powers (if possible) and/or cooling (if necessary). Or, due to the integrative capabilities of confined optical structures, this heating effect could be leveraged in an energy harvesting framework [27].

In seeking an effective modulation speed, we endeavored to minimize the resistance-capacitance (RC) time constant of the MQW modulator. For this, the resistance is defined by the impedance of the coupled transmission line, $R = 50\ \Omega$, while the capacitance is defined by $C \approx \varepsilon_r \varepsilon_0 A/t \approx 0.4$ nF, where $\varepsilon_r \approx 11$ is the dielectric constant, ε_0 is the permittivity of free space, $A \approx 12.5$ cm^2 is the area, and $t \approx 300$ μm is the thickness. The resulting time constant of $RC \approx 20$ ns is short, but it could be reduced by minimizing the area. For example, discrete/isolated MQW modulators could be patterned only over the microspheres' paraxial areas, rather than the full retro-modulator surface. This would decrease the time constant by the aforementioned ratio A_{PX}/A_{RM}. However, this benefit should be weighed against the added complexity of patterning and addressing discrete/isolated MQW modulators over the arrayed microspheres.

In seeking effective error performance in the links, we recognize that the geometric loss from the retro-modulator surface, due to the divergence detailed above, should be considered with turbulence-induced distortion from the link. While the characteristics and impacts from turbulent links are beyond the scope of this work, we can describe trends and limits for the retro-modulator surface's error performance through weak, moderate, and strong turbulence. (This was done using the turbulence emulator and procedures detailed in Appendix B.) We evaluated the retro-modulator surface's error performance via extracted error vector magnitude (EVM) values and bit error rates (BERs), towards a goal of keeping the BER below 10^{-3} (in the absence of forward error correction [28]). For weak, moderate, and strong turbulence, we measured EVMs of 3.7%, 9.2%, and 24%. We also found that the BERs for weak and moderate turbulence are below 10^{-3}, while the BER for strong turbulence rises above this limit (to 0.0183). This suggests that one or more of the above improvements to the retroreflection and/or modulation would need to be carried out to allow the retro-modulator surface to function through strong turbulence.

V. Conclusion

In this work, we introduced retro-modulator surfaces as monolithic passive transceivers, in active-passive links, and put forward analyses of their retroflection and modulation, given operation in the optical communication C-band (1530–1565 nm) with digital voltages (0–5 V). We then presented full characterizations of the devices with LaSFN9- or $BaTiO_3$-based microspheres in their sublayer and an overlying AlGaInAs-based MQW modulator. The retro-modulator surface with LaSFN9 ($n \approx 1.8$) microspheres was effective for shorter (e.g., indoor/terrestrial) links, across which it could offer retroreflection over a 10.8° field-of-view and modulation at a depth of 3.4%. In contrast, the retro-modulator surface with $BaTiO_3$ ($n \approx 2.0$) microspheres showed effectiveness for longer (e.g., aerial/aerospace) links, for which it could enable retroreflection over a 9.4° field-of-view and modulation at a depth of 5.3%. Such functionality for the devices, along with their reduced SWaP demands, can make the retro-modulator surfaces effective elements for future optical wireless and FSO communication systems.

Appendix A

This appendix provides additional details on the ray-based analysis used to calculate the retroreflectance $R_R(n,\theta)$.

Fig. A-1 shows a cross-section of a retroreflecting microsphere (in light blue), subtended by its optical axis, with incident and retroreflected rays above and below the optical axis, respectively. The incident rays propagate towards the microsphere, while parallel to its optical axis, and then enter its front surface and focus onto its rear surface. The retroreflected rays are formed by the resulting reflections, which return through the microsphere, exit its front surface, and propagate towards the receiver with varying degrees of divergence away from the optical axis. Given the varying divergence, we define our paraxial rays (in bright red) as the incident and retroreflected rays that are focused sufficiently close to the microsphere's rear vertex to later be captured by the receiver's aperture. Conversely, we define our nonparaxial rays (in light red) as the incident and retroreflected rays that focus further from the microsphere's rear vertex and are thus not captured by the receiver's aperture.

We then use our system of rays to quantify the retroreflectance $R_R(n,\theta)$ for a microsphere with a diameter $d = 56$ μm, a receiver aperture with a diameter $D = 25.4$ mm, and a length $L = 0.4$ m between the microsphere and receiver. This is done by considering a single microsphere and identifying its outermost paraxial (incident) ray. This ray strikes the microsphere further from the optical axis than all other paraxial (incident) rays, undergoes retroreflection through the microsphere, and then propagates to the receiver, where it is captured at the outer edge of the aperture. We circumscribe this outer paraxial (incident) ray around the optical axis and define the interior as the microsphere's paraxial cross-sectional area $A_{PX}(n)$. This area $A_{PX}(n)$ can be seen as the central (circular) area within the microsphere's greater (circular) cross-section, for which the incident rays will all later be captured by the receiver's aperture. For our microspheres of LaSFN9 and $BaTiO_3$, with refractive indices of $n \approx 1.8$ and 2.0, respectively, our ray-based analysis gives paraxial cross-sectional areas of $A_{PX}(n{=}1.8) \approx 0.21d^2$ and $A_{PX}(n{=}2.0) \approx 0.27d^2$, respectively. We then use the microsphere's total cross-sectional area $A_{MS} = (\pi/4)d^2 \approx 0.79d^2$ to define the ratio $A_{PX}(n{=}1.8)/A_{MS} \approx 0.27$ and $A_{PX}(n{=}2.0)/A_{MS} \approx 0.34$, respectively. This ratio $A_{PX}(n)/A_{MS}$ can be seen as the fraction of incident optical power on a microsphere that will be captured by the receiver's aperture, while ignoring reflective/absorptive loss from the microsphere and MQW modulator.

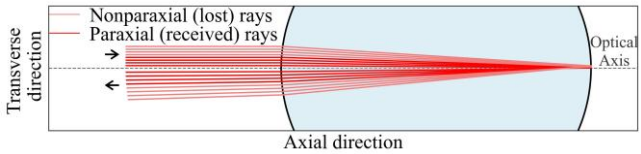

Fig. A-1. Ray-based analysis of a microsphere (in light blue), subtended by an optical axis, and transverse and axial directions. Incident rays propagate towards the microsphere (above and parallel to the optical axis), enter its front surface, and focus onto its rear surface. Retroreflected rays then return through the microsphere, exit its front surface, and propagate towards the receiver (below and diverging away from the optical axis). The incident and retroreflected rays that focus sufficiently close to the rear vertex to later be captured by the receiver's aperture are the paraxial rays (in bright red); the incident and retroreflected rays that focus further from the rear vertex and are not captured by the receiver's aperture are the nonparaxial rays (in light red).

APPENDIX B

This appendix characterizes the retro-modulator surface's error performance via EVM and BER measurements of optical wireless and FSO links subject to turbulence.

Fig. B-1 shows the experimental setup that characterizes our device performance through weak, moderate, and strong turbulence. The setup includes a *fixed transceiver* that we built for intensity modulation/direct detection (IM/DD), via amplitude modulation/reception, or coherent detection, via amplitude and phase modulation/reception. It also includes a *mobile transceiver* with our retro-modulator surface. Given that our retro-modulator surface applies only amplitude modulation, we restrict the former transceiver to IM/DD operation. This has its displayed red beam propagate from the laser (Thorlabs Inc., TL1X) to the half-wave plate HWP_1 (Thorlabs Inc., AHWP10M-1600), to form a well-polarized beam, and then through the non-polarizing beamsplitter cube BS (Thorlabs Inc., CCM1-BS015 /M). The beam then propagates through our turbulent channel. The turbulence is applied by a turbulence emulator with a rotating phase plate, through which differing levels of turbulence-induced distortion are applied. The distorted beam then reaches the mobile transceiver, reflects off its flip-mount mirror FMM, and strikes the infrared camera (New Imaging Technologies S.A.S., WiDy SenS 640V-ST), which captures images of the turbulence-induced distortion on the transverse beam intensity. As warranted, we retract the flip-mount mirror FMM to let the distorted beam propagate to the retro-modulator surface. The modulated and retroreflected beam then returns through the turbulent channel and reaches the fixed transceiver. In the transceiver, the beam reflects off the beamsplitter cube BS and passes through the half-wave plate HWP_2 (Thorlabs Inc., AHWP10M-1600), which is configured for IM/DD operation by having its fast axis aligned with the beam's polarization. The beam is then transmitted fully through the polarizing beamsplitter cube PBS (Thorlabs Inc., CCM1-PBS25-1550/M) and onto photodiode PD_2 (Thorlabs Inc., PDB210C/M). The resulting photocurrent is recorded as a function of time by an oscilloscope (Tektronix Inc., TDS2004B) and characterized via EVM, being the normalized root mean square error of the expected and received photocurrents as a percentage. We use the metrics of EVM and BER here, as we lack the ability to measure the very low BERs from links with weak and moderate turbulence.

Fig. B-2 displays the transverse beam intensity recorded by the infrared camera, shown in the left column as a function of the horizontal *x* and vertical *y* dimensions, and the corresponding constellation histograms, shown in the right column as the frequency of occurrence for a 0-bit (in blue) or 1-bit (in red). The results are presented for FSO channels experiencing weak turbulence in (a) and (b), moderate turbulence in (c) and (d), and strong turbulence in (e) and (f). For weak turbulence, we see the desired transverse beam intensity in (a), with a near-ideal Gaussian profile, and the desired distributions of bits in (b), with the 0-bit (blue) and 1-bit (red) having tightly packed Gaussian distributions. These near-ideal conditions yield an especially low EVM of 3.7%. For moderate turbulence, we see the manifestation of low-order distortion on the transverse beam intensity in (c), as slow spatial variations in intensity across the profile, and the growing potential for bit errors in (g), as the 0-bit (blue) and 1-bit (red) have widened distributions. These conditions lead to an increased EVM, at 9.2%. For strong turbulence, we see the emergence of high-order distortion on the transverse beam intensity in (e), as high spatial variations in intensity across the profile, and obvious bit errors in (f), as the 0-bit (blue) and 1-bit (red) have overlapping distributions. Such undesirable conditions lead to an EVM of 24%. From established practices [28], we define a maximum BER of 10^{-3} for communication prior to applying forward error correction. As mentioned above, we lack the ability to measure the especially low BERs from communication through weak and moderate turbulence, but we can confirm that the measured BERs for these conditions are below 10^{-3}. Thus, the retro-modulator surface is deemed to function effectively through weak and moderate turbulence. For FSO links through strong turbulence, however, the rate of errors grows unacceptably high, and reaches a BER of 0.0183. In such conditions, turbulence mitigation would be warranted via techniques based upon adaptive optics [29], [30], pilot-assisted communications [31–35], optical phase conjugation [36–38], orbital angular momentum and vector beams [39–41], and the like.

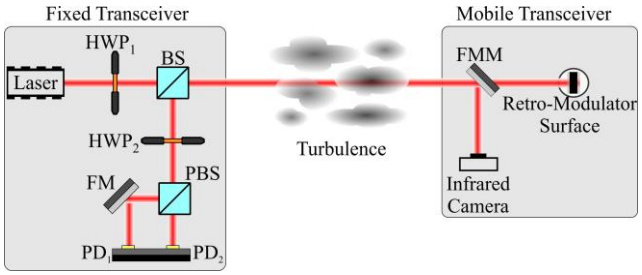

Fig. B-1. Experimental setup used to characterize the retro-modulator surface's error performance through weak, moderate, and strong turbulence. It includes a fixed transceiver on the left and a mobile transceiver with the retro-modulator surface on the right. The displayed beam (in red) propagates from the laser through the half-wave plate HWP_1 and beamsplitter cube BS. It then propagates through a turbulent channel, as defined by a turbulence emulator with a rotating phase plate. The distorted beam reaches the mobile transceiver, where the flip-mount mirror FMM has the beam strike the infrared camera or retro-modulator surface. The modulated and retroreflected beam returns through the turbulent channel and reaches the generalized transceiver, where it reflects off the beamsplitter cube BS, passes through the half-wave plate HWP_2, transmits fully through the polarizing beamsplitter cube PBS, and strikes photodiode PD_2.

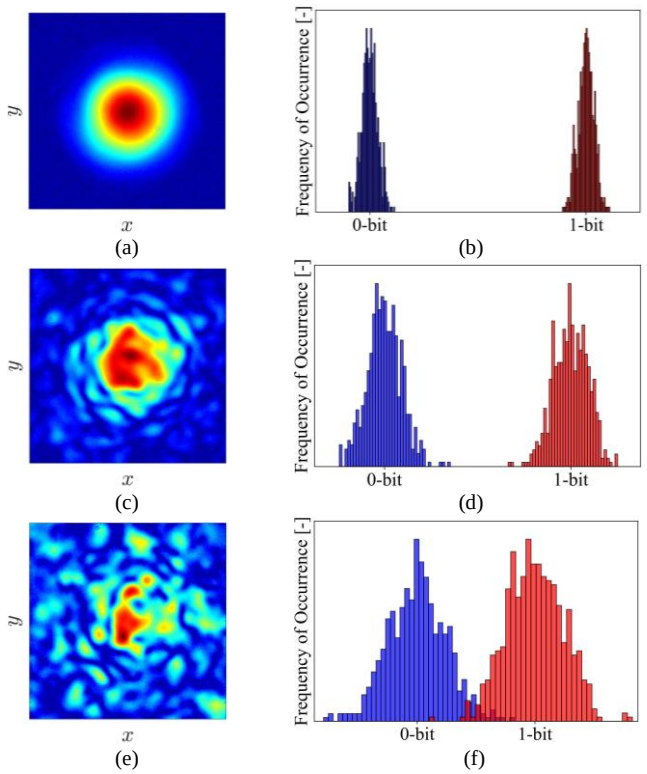

Fig. B-2. The transverse beam intensity recorded by the infrared camera, shown in the left column as a function of the horizontal *x* and vertical *y* dimensions, and the corresponding constellation histograms, shown in the right column as the frequency of occurrence for a 0-bit (in blue) or 1-bit (in red). Results are presented for channels exhibiting weak turbulence in (a) and (b), moderate turbulence in (c) and (d), and strong turbulence in (e) and (f).

ACKNOWLEDGMENT

The authors thank the Fipke Laboratory for Trace Element Research (FiLTER) at the University of British Columbia for aiding with the scanning electron microscope (SEM) images.

REFERENCES

[1] Y. Chang, Z. Liu, H. Yao, T. Geng, Y. Chen, and S. Liu, "Research on 4-pam signal compensation technology for high-speed indoor FSOC based FNN," *Proc. SPIE*, vol. 12306, pp. 1–5, Aug. 2022.
[2] S. Bibi, M. I. Baig, F. Qamar, and R. Shahzadi, "A comprehensive survey of free-space optical communication – modulation schemes, advantages, challenges and mitigations," *J. Opt. Commun*., vol. 45, pp. s2373–s2385, Oct. 2023.
[3] H. Henniger and O. Wilfert, "An introduction to free-space optical communications," *Radioengineering*, vol. 19, pp. 203–212, Jun. 2010.
[4] F. A. Dahri, F. A. Umrani, K. Memon, F. Memon, and A. W. Umrani, "Performance analysis of modulation techniques for indoor free space optics," *J. Appl. Eng. Technol*., vol. 8, pp. 72–80, Jun. 2024.
[5] W. S. Rabinovich *et al*., "45-Mbit/s cat's-eye modulating retroreflectors," *Opt. Eng*., vol. 46, Art. no. 104001, Oct. 2007.
[6] Y. Zhang, Y. Wang, Y. Deng, A. Du, and J. Liu, "Design of a free space optical communication system for an unmanned aerial vehicle command and control link," *Photonics*, vol. 8, no. 5, Art. no. 163, May 2021.
[7] J. Poliak, R. M. Calvo, and F. Rein, "Demonstration of 1.72 Tbit/s optical data transmission under worst-case turbulence conditions for ground-to-geostationary satellite communications," *IEEE Commun. Lett*., vol. 22, no. 9, pp. 1818–1821, Sept. 2018.
[8] C. Marxer *et al*., "Reflective duplexer based on silicon micromechanics for fiber-optic communication," *J. Lightwave Technol*., vol. 17, no. 1, pp. 115–122, Jan. 1999.
[9] J. Zhu *et al*., "First demonstration of a WDM-PON system using full C-band tunable SFP+ transceiver modules," *J. Opt. Commun. Netw*., vol. 7, no. 1, pp. A28–A36, Jan. 2015.
[10] D. Gao *et al*., "Multi-modulation compatible miniaturization system for FSO communication assisted by chirp-managed laser," *Opt. Express*, vol. 30, pp. 32306-32316, Aug. 2022.
[11] E. Rosenkrantz and S. Arnon, "1500 nm modulating retroreflector based on coated nanoparticles for free-space optical communication," *Appl. Opt.*, vol. 54, no. 17, pp. 5309–5313, Jun. 2015.
[12] A. C. MacGillivray, S. Gorgani, I. R. Hristovski, M. F. Jenne, N. I. Lesack, and J. F. Holzman, "A novel hemispherical retro-modulator for free-space optical communication links," *IEEE Photonics Technol. Lett*., vol. 34, no. 9, pp. 494–497, May 2022,
[13] B. Born, I. R. Hristovski, S. Geoffroy-Gagnon, and J. F. Holzman, "All-optical retro-modulation for free-space optical communication," *Opt. Express*, vol. 26, no. 4, pp. 5031–5042, Feb. 2018.
[14] C. Chen, J. Ji, H. Zhao, and Y. Song, "Performance analysis and experimental evaluation of modulating retroreflector and UAV based free space optical transmission systems," *Opt. Express*, vol. 32, no. 19, pp. 33830–33851, Sept. 2024.
[15] G. Gilbreath *et al*., "Progress in development of multiple-quantum-well retromodulators for free-space data links," *Opt. Eng*., vol. 42, no. 6, pp. 1611–1617, Jun. 2003.
[16] W. S. Rabinovich *et al*., "Free space quantum key distribution using modulating retro-reflectors," *Opt. Express*, vol. 26, no. 9, pp. 11331–11351, Apr. 2018.
[17] P. G. Goetz *et al*., "Modulating retro-reflector lasercom systems for small unmanned vehicles," *IEEE J. Sel. Areas Commun*., vol. 30, no. 5, pp. 986–992, Jun. 2012.
[18] D. A. B. Miller *et al*., "Band-edge electroabsorption in quantum well structures: The quantum-confined Stark effect," *Phys. Rev. Lett.*, vol. 53, pp. 2173–2176, Nov. 1984.
[19] ASTM International, "ASTM International Standard E808 – 23, Standard Practice for Describing Retroreflection," Term 3.2.17, Dec. 2023.
[20] G. Mie, "Beiträge zur optik trüber medien, speziell kolloidaler metallösungen," *Ann. Phys*., vol. 330, no. 3, pp. 377–445, 1908.
[21] B. Born, J. D. A. Krupa, S. Geoffroy-Gagnon, and J. F. Holzman, "Integration of photonic nanojets and semiconductor nanoparticles for enhanced all-optical switching," *Nat. Commun*., vol. 6, Art. no. 8097, Aug. 2015.
[22] Y. E. Geints, E. K. Panina, and A. A. Zemlyanov, "Control over parameters of photonic nanojets of dielectric microspheres," *J. Opt. Commun*., vol. 283, no. 23, pp. 4775–4781, Dec. 2010.
[23] M. Born and E. Wolf, "Principles of Optics: Electromagnetic Theory of Propagation, Interference and Diffraction of Light," 7th ed. Cambridge, Cambridge University Press, 1999.
[24] M. Fox, "Quantum Optics: An Introduction," Oxford, Oxford University Press, 2006.
[25] Shilpa Enterprises, *"ITO Coated Glass – Transparent Conductive Glass Substrate,"* Shilpent, [Online]. Available: https://shilpent.com/conductive-glass/50-ito-coated-glass.html [Accessed: Nov. 10, 2025].
[26] A. C. MacGillivray, N. I. Lesack, I. R. Hristovski, M. F. Jenne, B. C. Maglio, S. Gorgani, and J. F. Holzman, "Band-edge absorption characteristics of semi-insulating indium phosphide under unified Franz-Keldysh and Einstein models," *Phys. Rev. B*., vol. 105, Art. no. 155203, Apr. 2022.
[27] M. de Cea, A. H. Atabaki, and R. J. Ram, "Energy harvesting optical modulators with sub-attojoule per bit electrical energy composition," *Nat. Commun*., vol. 12, Art. no. 2361, Apr. 2021.
[28] *Forward Error Correction for High Bit-Rate DWDM Submarine Systems*, ITU-T Recommendation *G.975.1*, International Telecommunications Union, Geneva, Switzerland, Feb. 2004.
[29] R. K. Tyson, "Bit-error rate for free-space adaptive optics laser communications," *J. Opt. Soc. Am. A*, vol. 19, no. 4, pp. 753–758, May 2002.
[30] Y. Ata and M.-S. Alouini, "HAPS based FSO links performance analysis and improvement with adaptive optics correction," *IEEE Trans. Wirel. Commun.*, vol. 22, no. 7, pp. 4916–4929, July 2023.
[31] R. Zhang *et al*., "Turbulence-resilient pilot-assisted self-coherent free-space optical communications using automatic optoelectronic mixing of many modes," *Nat. Photon.*, vol. 15, pp. 743–750, Sept. 2021.
[32] H. Zhou *et al*., "Demonstration of turbulence resiliency in a mode-, polarization-, and wavelength-multiplexed free-space optical link using pilot-assisted optoelectronic beam mixing," *J. Light. Technol.*, vol. 40, no. 3, pp. 588–596, Feb. 2022.
[33] H. Zhou *et al*., "Demonstration of turbulence-resilient self-homodyne 12-Gbit/s 16-QAM free-space optical communications using a transmitted pilot tone," *J. Light. Technol.*, vol. 41, no. 11, pp. 3438–3445, June 2023.

[34] R. Zhang *et al.*, "Automatic turbulence resilience in pilot-assisted self-coherent free-space optical communications," *J. Light. Technol.*, vol. 42, no. 10, pp. 3760–3769, May, 2024.
[35] D. McDonald, R. Bellossi, and S. Gładysz, "Field demonstration of turbulence-resilient self-coherent free-space optical communications," *J. Light. Technol.*, vol. 43, no. 13, pp. 6146–6153, July 2025.
[36] H. Zhou *et al.*, "Automatic turbulence mitigation for coherent free-space optical links using crystal-based phase conjugation and fiber-coupled data modulation," *Opt. Lett.*, vol. 48, no. 8, pp. 2194–2197, Apr. 2023.
[37] S. Singh *et al.*, "Light correcting light with nonlinear optics," *Adv. Photonics*, vol. 6, no. 2, Feb. 2024, Art. no. 026003.
[38] H. Zhou *et al.*, "Automatic mitigation of dynamic atmospheric turbulence using optical phase conjugation for coherent free-space optical communications," *Optica*, vol.12, no. 2, pp.158–167, Feb. 2025.
[39] Z. Zhu *et al.*, "Compensation-free high-dimensional free-space optical communication using turbulence-resilient vector beams," *Nat. Commun.*, vol. 12, Mar. 2021, Art. no. 1666.
[40] Y. Yu *et al.*, "Demonstration of 120 Gbit/s turbulence-resilient coherent optical communication employing cylindrical vector beam multiplexing," *Opt. Express*, vol. 31, no. 25, pp. 42165–42175, Dec. 2023.
[41] Z. Song *et al.*, "High capacity turbulence-resilient free-space chaotic optical communication based on vector optical field manipulation," *J. Light. Technol.*, vol. 42, no. 24, pp. 8647–8654, Dec. 2024.